The ASTER Global Emissivity Dataset (GED) Version 4.1

Monthly 0.05º Product 2000-2015

==========

Produced by: Glynn Hulley

Jet Propulsion Laboratory, California Institute of Technology

Pasadena, CA

Contact: glynn.hulley@jpl.nasa.gov

Version: 4.1**

Description and Availability:

https://lpdaac.usgs.gov/dataset_discovery/community/community_products_table

Reference:

Hulley, G., Hook S.J, Abbott, E., Malakar, N., Islam, T., Abrams, M., (2015), The ASTER Global Emissivity Database (ASTER GED): Mapping Earth's emissivity at 100 meter spatial resolution, *Geophysical Research Letters*, 42, doi:10.1002/2015GL065564.

** In 4.1 georeferencing attributes have been added to the SDS Group in addition to product specific attributes such as scaling, offsets and datatypes. Please see section 4.1 for a list of these attributes.

==========

1. Introduction

Using data from the Advanced Spaceborne Thermal Emission and Reflection Radiometer (ASTER) on NASA's Terra spacecraft, NASA/JPL recently released the most detailed global emissivity map of the Earth termed the ASTER Global Emissivity Database (ASTER GEDv3), available at https://lpdaac.usgs.gov/products/community_products_table. ASTER GEDv3 was created by processing millions of cloud free ASTER data from 2000-2008 and calculating an average emissivity of the surface at ~100 m spatial resolution at the five ASTER TIR wavelengths (Hulley et al. 2015). Validation over a global set of sites showed a close match in spectral shape with lab measured spectra, and average band error of ~1% (Hulley et al. 2015; Hulley et al. 2009).

Since the ASTER-GEDv3 emissivities are static (mean from 2000-2008), an emissivity adjustment was necessary to account for land surface changes over heterogeneous land cover types that are subject to annual and inter-annual variability; for example, due to snow and ice melt, agricultural practices, and droughts. The emissivity over desert regions will remain invariant over time in the absence of soil moisture. To account for these changes, a monthly mean ASTER GEDv4 emissivity product at 0.05° resolution has been produced from 2000-2015 by using snow cover data from the standard monthly MODIS/Terra snow cover monthly global 0.05 deg product (MOD10CM), and vegetation information from the MODIS monthly gridded NDVI product (MOD13C2). The methodology for producing the monthly mean product including uncertainty is described below

2. Methodology

The emissivity of vegetation and snow is high and constant (~0.98-1.0) across the TIR range from 8-12 µm, and as a result vegetation or snow cover systematically reduces the amount of spectral variation in emissivity for a given surface. *Valor and Caselles,* (1996) initially proposed a theoretical relationship between emissivity and NDVI based on observations made by *van de Griend and Owe* (1993), and various forms of this method have been adapted to routinely estimate emissivity for LST estimation from sensors including Advanced Very High Resolution Radiometer (AVHRR) (Sobrino and Raissouni 2000), ASTER (Jiménez-Muñoz et al. 2006),

Landsat (Sobrino et al. 2004) and (Advanced) Along Track Scanning Radiometer (A)ATSR (Kogler et al. 2012). The emissivity-NDVI relationship is based on a theoretical approach in which the emissivity, ε_λ, of a mixed pixel (NDVI values between ~0.2 and 0.5) can be described as a linear relationship between the bare soil and vegetation fraction (Sobrino et al. 1990):

$$\varepsilon_\lambda = \varepsilon_{\lambda,v} f_v + \varepsilon_{\lambda,s}(1 - f_v) \quad (1)$$

Where $\varepsilon_{\lambda,v}$ and $\varepsilon_{\lambda,s}$ are the emissivity of the vegetation and bare soil respectively at some wavelength, λ, and f_v is the vegetation cover fraction (Carlson and Ripley 1997):

$$f_v = 1 - \frac{NDVI_{max} - NDVI}{NDVI_{max} - NDVI_{min}} \quad (2)$$

Where $NDVI_{max}$ and $NDVI_{min}$ are NDVI values for the full vegetation and bare soil components respectively on the scene. *Valor and Caselles*, 1996 concluded that emissivity can be calculated with an absolute error of 1-2 % for mixed vegetation pixels, decreasing to 0.7-1 % for fully vegetated pixels, with a mean error being of the order of 1 %.

Since ASTER GED includes the mean emissivity and NDVI (calculated from visible ASTER data bands), the adjustment approach first involves estimating the bare soil component for the ASTER pixel, and adjusting this value based on the vegetation information at the time of interest from an external data source, e.g. MODIS. The bare soil fraction for each band is estimated by apportioning the emissivity according to the fractional vegetation cover estimated from the mean ASTER NDVI product as follows:

$$\varepsilon_{ASTER,bare} = \frac{\varepsilon_{ASTER} - \varepsilon_{veg}\, f_{v,ASTER}}{1 - f_{v,ASTER}} \quad (3)$$

Where ε_{ASTER} is the ASTER-GEDv3 emissivity, $\varepsilon_{ASTER,bare}$ is the ASTER bare soil emissivity component, ε_{veg} is an average vegetation emissivity spectrum from the ASTER spectral library (Baldridge et al. 2009), and $f_{v,ASTER}$ is the ASTER vegetation cover fraction computed using (2).

Next, the vegetation adjusted ASTER emissivity is estimated based on the bare pixel component from (3) and the vegetation cover fraction derived from MODIS for the time period of interest (e.g. monthly mean);

$$\varepsilon'_{ASTER} = f_{v,MODIS}\, \varepsilon_{veg} + \left(1 - f_{v,MODIS}\right) \varepsilon_{ASTER,bare} \quad (4)$$

Where ε'_{ASTER} is the adjusted ASTER emissivity for vegetation, and $f_{v,MODIS}$ is the vegetation cover fraction estimated from MODIS data using (2). The final step involves an additional adjustment for percent snow cover using the same linear adjustment procedure as in the previous step:

$$\varepsilon''_{ASTER} = f_{s,MODIS}\,\varepsilon_{snow} + (1 - f_{s,MODIS})\varepsilon'_{ASTER} \qquad (5)$$

Where ε''_{ASTER} is the vegetation and snow adjusted ASTER-GEDv4 emissivity, and $f_{s,MODIS}$ is the MODIS snow cover fraction. Data from the global monthly MODIS snow cover 0.05° product (MOD10CM), and the MODIS monthly gridded NDVI product (MOD13C2) were used to estimate $f_{v,MODIS}$ and $f_{s,MODIS}$ in (4) and (5).

An example of the adjusted ASTER GEDv4 monthly product for the year 2004 with corresponding uncertainty is shown in Figure 1 for March (top), June (middle) and September (bottom) 2004 for band 12 (9.1 μm). Uncertainties are given in absolute percent (%). Note the largest uncertainties are over regions that had the largest seasonal changes in phenology (e.g. Sahel), and over semi-arid regions (Australian outback). Uncertainties are lowest over desert landscapes and over fully covered snow regions (Greenland).

Figure 2 shows an additional example focused on two regions, highlighting changes due to snow cover over the Rocky Mountains in Colorado, USA, and due to vegetation phenology over the Sahel region in Senegal, North Africa. Over the Sahel region (Figure 2a), emissivities over the grasslands are lower during the dry period in March when grasses are in a senesced and dry state, but an increase in emissivity can clearly be seen during June and September due to summertime rainfall that results in greener and denser vegetation cover that is more evident along the fringes of desert and grassland regions in the north of the images. Corresponding emissivity uncertainty in % (Figure 2b) are highest over pixels that had the largest vegetation adjustment based on (4). Higher emissivities (bright red) during January over the Rockies (Figure 2c) are a result of increased wintertime snow cover at high elevations, while a decrease in emissivity can be seen in subsequent months of March and June due to snowmelt and subsequent exposure to background vegetation (orange) and rocks (blue) during the warmer melt periods. Corresponding emissivity uncertainties (Figure 2d) are highest over pixels that had the largest snow adjustment based on (5).

3. Uncertainty Analysis

A Temperature Emissivity Uncertainty Simulator (TEUSim) was developed at JPL for simulating LST&E uncertainties from various sources of error for the TES algorithm using in the creation of ASTER GED in a rigorous manner for any appropriate TIR sensor (Hulley et al. 2012). These include random errors (noise), systematic errors (calibration), and spatio-temporally correlated errors (atmospheric). The MODTRAN 5.2 radiative transfer model was used for the simulations with a global set of radiosonde profiles and surface emissivity spectra representing a broad range of atmospheric conditions and a wide variety of surface types. This approach allows the retrieval algorithm to be easily evaluated under realistic but challenging combinations of surface/atmospheric conditions. The TEUSim is designed to separately quantify error contributions from the following potential sources: noise, model, atmospheric correction, undetected cloud, calibration.

A set of global radiosonde profiles from the SeeBor database were adjusted to simulate real data by applying estimated uncertainties from the MODIS MOD07 atmospheric product (Seemann et al. 2006; Seemann et al. 2003). Using a dataset of 80 clear sky cases over the SGP ARM site (Tobin et al. 2006), MOD07 air temperature RMS errors showed a linearly decreasing trend from 4 K at the surface to 2 K at 700 mb, and a constant 2 K above 700 mb (Seemann et al. 2006). These reported values were used to perturb the air temperature profiles at each associated level using a random number generator with a mean centered on the RMS error. The uncertainty of the water vapor retrievals were estimated to be between 10–20% (Seemann et al. 2006). Accordingly, the relative humidity profiles were adjusted by scaling factors ranging from 0.8 to 1.2 in MODTRAN using a uniformly distributed random number generator.

The total emissivity uncertainty for band *i* in the TES algorithm based on model, atmospheric and measurement noise contributions can be written as:

$$\delta\varepsilon_{i,TES} = \left[\delta\varepsilon_{i,M} + \delta\varepsilon_{i,A} + \delta\varepsilon_{i,N}\right]^{1/2} \quad (6)$$

where $\delta\varepsilon_{i,M}$ is the model error due to assumptions made in the TES calibration curve, $\delta\varepsilon_{i,A}$ is the atmospheric error, and $\delta\varepsilon_{i,N}$ is the error associated with measurement noise. These errors are assumed to be independent.

The second uncertainty source in ASTER GEDv4 is due to the monthly adjustment based on MODIS vegetation and snow cover information. This uncertainty was estimated as the magnitude of the difference in emissivity from the adjustment, multiplied by the uncertainty based on the theoretical emissivity/NDVI relationship (Valor and Caselles 1996).

$$\delta\varepsilon_i' = (\varepsilon_i' - \varepsilon_i) \cdot \delta\varepsilon_i \quad (7)$$

Where ε_i' is the adjusted emissivity from (4), ε_i is the original ASTER GEDv3 retrieved emissivity, and $\delta\varepsilon_i$ is the uncertainty in the emissivity/NDVI relationship for band *i*. Valor and Caselles, 1996 concluded that emissivity can be calculated with an absolute error of 1-2 % for mixed vegetation pixels, decreasing to 0.5-1 % for fully vegetated pixels, with a mean error being of the order of 1 %. In ASTER GEDv4 we assumed a maximum uncertainty of 2% for mixed pixels defined as having an NDVI between 0.2 and 0.5, and a minimum uncertainty of 0.5% for fully vegetated pixels having an NDVI greater than 0.8. Uncertainties were then linearly interpolated between these NDVI assigned values to estimate $\delta\varepsilon_i$. Pixels that had large changes in emissivity due to the adjustment had correspondingly larger uncertainties, particularly over mixed pixels. Uncertainties due to adjustment, $\delta\varepsilon_i'$, were set to zero over arid pixels (NDVI<0.2), so over most desert landscapes the total uncertainty was only due to algorithm uncertainty given by (6).

The total uncertainty per band and per pixel is then calculated as a combination of (6) and (7) as follows:

$$\delta\varepsilon_{i,tot} = \sqrt{\delta\varepsilon_i'^2 + \delta\varepsilon_{i,TES}^2} \quad (7)$$

Any studies using ASTER GEDv4 should include this uncertainty in their calculations and analysis. Future work will involve an additional adjustment over desert regions due to changes in soil moisture, which reduces the spectral contrast in emissivity and can result in large variations

in the quartz bands (ASTER bands 10-12) (Hulley et al. 2010; Mira et al. 2007). Soil moisture information can be derived from microwave remote sensing measurements of top layer soil moisture, e.g. SMAP, SMOS, or AMSR-E.

4. Product Format and Description

Table 1. The Scientific Data Sets (SDSs) in the ASTER GEDv4 product in hdf5 format

SDS	Long Name	Data type	Units	Valid Range	Fill Value	Scale Factor	Offset
Emissivity	Band 10 - 8.3 μm Band 11 - 8.6 μm Band 12 - 9.1 μm Band 13 - 10.6 μm Band 14 - 11.3 μm	uint8	n/a	1-255	0	0.002	0.49
Emissivity Uncertainty	Band 10 - 8.3 μm Band 11 - 8.6 μm Band 12 - 9.1 μm Band 13 - 10.6 μm Band 14 - 11.3 μm	uint8	n/a	1-255	0	0.002	n/a
NDVI	Normalized Difference Vegetation Index (MOD13C2)	uint16	n/a	0-65535	0	0.001	n/a
QFlag	Quality Flag: 0 = Land 1 = Filled value 2 = Ocean	uint8	n/a	0-255	n/a	n/a	n/a

4.1 Product Attributes

```
Group '/SDS'
  Attributes:
    'GridName':  'ASTER_GEDv4.1_0.05DEG_CMG_EMIS'
```

'XDim': 7200.000000
'YDim': 3600.000000
'UpperLeftPointMtrs': '(-180000000.000000,90000000.000000)'
'LowerRightPointMtrs': '(180000000.000000,-90000000.000000)'
'Projection': 'GCTP_GEO'
'GridOrigin': 'HDFE_GD_UL'
'EASTBOUNDINGCOORDINATE': 180.000000
'WESTBOUNDINGCOORDINATE': -180.000000
'SOUTHBOUNDINGCOORDINATE': -90.000000
'NORTHBOUNDINGCOORDINATE': 90.000000
Dataset 'Emissivity'
Size: 7200x3600x5
MaxSize: 7200x3600x5
Datatype: H5T_STD_U8LE (uint8)
ChunkSize: 7200x3600x5
Filters: none
FillValue: 0
Attributes:
'Description': 'Emissivity '
'Precision': 'uint8 '
'Scale Factor': 0.002000
'Offset': 0.490000
Dataset 'EmissivityUncertainty'
Size: 7200x3600x5
MaxSize: 7200x3600x5
Datatype: H5T_STD_U8LE (uint8)
ChunkSize: 7200x3600x5
Filters: none
FillValue: 0
Attributes:
'Description': 'Emissivity Uncertainty '
'Precision': 'uint8 '
'Scale Factor': 0.020000
'Offset': 0.000000
Dataset 'NDVI'
Size: 7200x3600
MaxSize: 7200x3600
Datatype: H5T_STD_I16LE (int16)
ChunkSize: 7200x3600
Filters: none
FillValue: 0
Attributes:
'Description': 'Normalized Difference Vegetation Index '
'Precision': 'uint16 '
'Scale Factor': 0.001000
'Offset': 0.000000
Dataset 'QualityFlag'
Size: 7200x3600
MaxSize: 7200x3600
Datatype: H5T_IEEE_F64LE (double)

ChunkSize: 7200x3600
Filters: none
FillValue: 0.000000
Attributes:
   'Description': 'Quality Flag '
   'Precision': 'uint8 '
   'Scale Factor': 0.000000
   'Offset': 0.000000

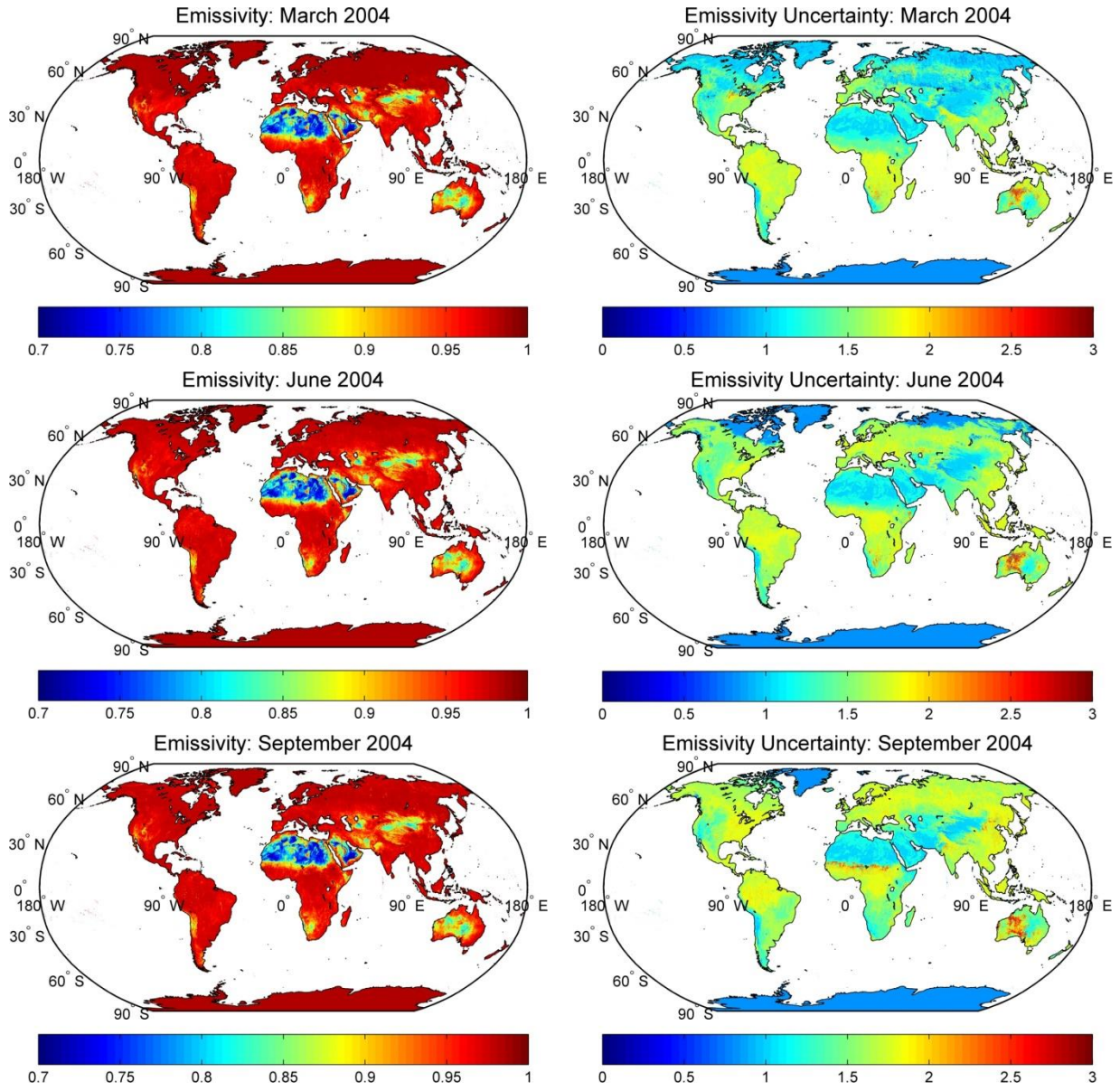

Figure 1. ASTER GEDv4 global emissivity with corresponding uncertainty for March (top), June (middle) and September (bottom) 2004 for band 12 (9.1 µm). Uncertainties are given in absolute percent (%). Note the largest uncertainties are over regions that had the largest seasonal changes in phenology (e.g. Sahel), and over semi-arid regions (Australian outback). Uncertainties are lowest over desert landscapes and over fully covered snow regions (Greenland).

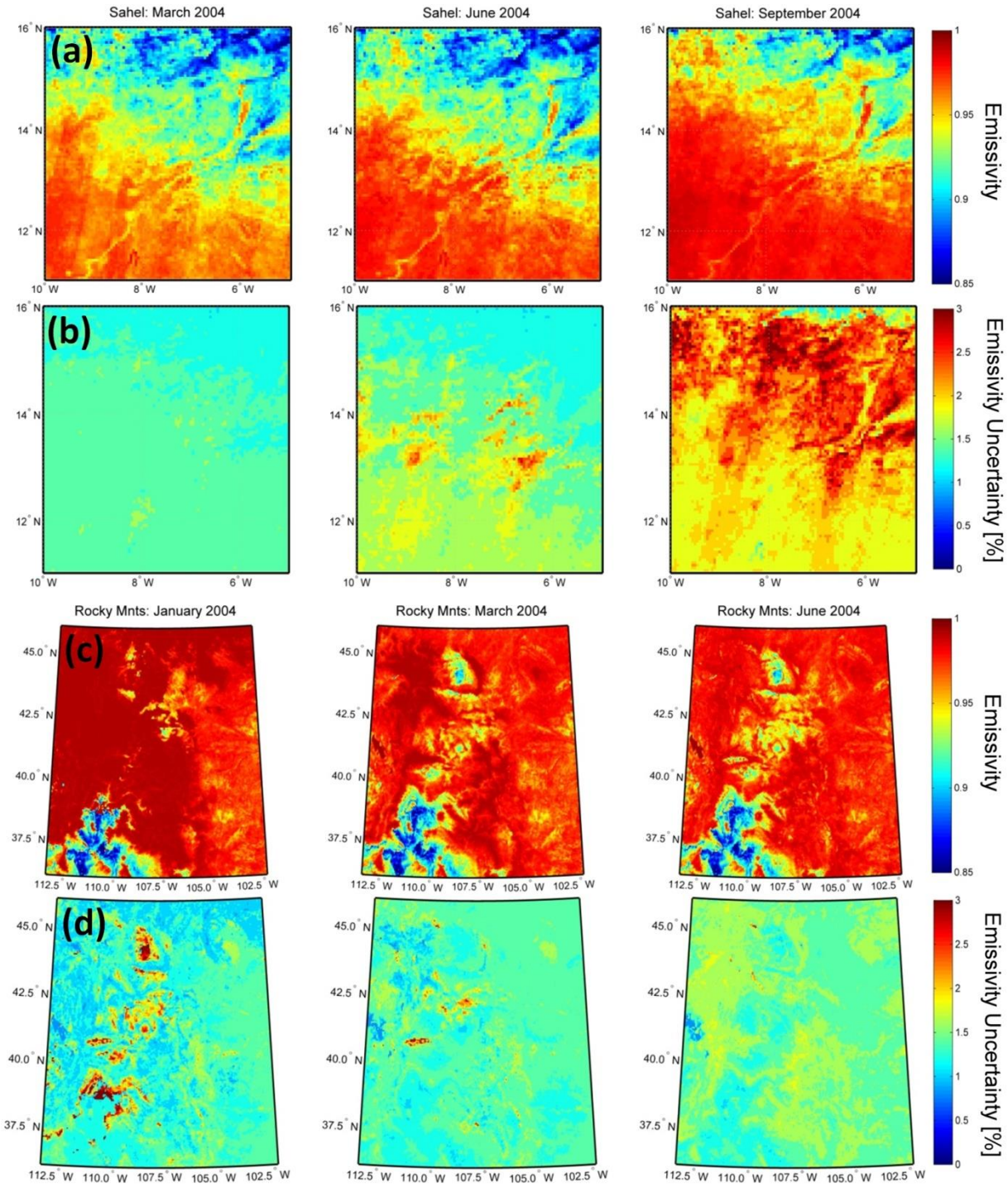

Figure 2. (a) ASTER GEDv4 monthly emissivity showing increasing emissivity due to vegetation green-up from summer rainfall over the Sahel, Senegal from Mar- Sep 2004, and (b) corresponding emissivity uncertainty estimate (%). (c) ASTER GEDv4 monthly emissivity showing decreasing emissivity with snowmelt from Jan-June 2004 over the Rocky Mountains in Colorado, and (d) corresponding emissivity uncertainty estimate (%).

5. References

Baldridge, A.M., Hook, S.J., Grove, C.I., & Rivera, G. (2009). The ASTER Spectral Library Version 2.0. *Remote Sensing of Environment, 114*, 711-715

Carlson, T.N., & Ripley, D.A. (1997). On the relation between NDVI, fractional vegetation cover, and leaf area index. *Remote Sensing of Environment, 62*, 241-252

Hulley, G.C., Hook, S.J., Abbott, E., Malakar, N., Islam, T., & Abrams, M. (2015). The ASTER Global Emissivity Dataset (ASTER GED): Mapping Earth's emissivity at 100 meter spatial scale. *Geophysical Research Letters, 42*, 7966-7976

Hulley, G.C., Hook, S.J., & Baldridge, A.M. (2009). Validation of the North American ASTER Land Surface Emissivity Database (NAALSED) Version 2.0 using Pseudo-Invariant Sand Dune Sites. *Remote Sensing of Environment, 113*, 2224-2233

Hulley, G.C., Hook, S.J., & Baldridge, A.M. (2010). Investigating the Effects of Soil Moisture on Thermal Infrared Land Surface Temperature and Emissivity Using Satellite Retrievals and Laboratory Measurements. *Remote Sensing of Environment, 114*, 1480-1493

Hulley, G.C., Hughes, C.G., & Hook, S.J. (2012). Quantifying uncertainties in land surface temperature and emissivity retrievals from ASTER and MODIS thermal infrared data. *Journal of Geophysical Research-Atmospheres, 117*

Jiménez-Muñoz, J.C., Sobrino, J.A., Gillespie, A., Sabol, D., & Gustafson, W.T. (2006). Improved land surface emissivities over agricultural areas using ASTER NDVI. *Remote Sensing of Environment, 103*, 474-487

Kogler, C., Pinnock, S., Arino, O., Casadio, S., Corlett, G., Prata, F., & Bras, T. (2012). Note on the quality of the (A)ATSR land surface temperature record from 1991 to 2009. *International Journal of Remote Sensing, 33*, 4178-4192

Mira, M., Valor, E., Boluda, R., Caselles, V., & Coll, C. (2007). Influence of soil water content on the thermal infrared emissivity of bare soils: Implication for land surface temperature determination. *Journal of Geophysical Research-Earth Surface, 112*, -

Seemann, S.W., Borbas, E., Li, J., Menzel, P., & Gumley, L.E. (2006). MODIS Atmospheric Profile Retrieval Algorithm Theoretical Basis Document, Cooperative Institute for Meteorological Satellite Studies, University of Wisconsin-Madison, Madison, WI, Version 6, October 25, 2006

Seemann, S.W., Li, J., Menzel, W.P., & Gumley, L.E. (2003). Operational retrieval of atmospheric temperature, moisture, and ozone from MODIS infrared radiances. *Journal of Applied Meteorology, 42*, 1072-1091

Sobrino, J.A., Caselles, V., & Becker, F. (1990). Significance of the Remotely Sensed Thermal Infrared Measurements Obtained over a Citrus Orchard. *Isprs Journal of Photogrammetry and Remote Sensing, 44*, 343-354

Sobrino, J.A., Jimenez-Munoz, J.C., & Paolini, L. (2004). Land surface temperature retrieval from LANDSAT TM 5. *Remote Sensing of Environment, 90*, 434-440

Sobrino, J.A., & Raissouni, N. (2000). Toward remote sensing methods for land cover dynamic monitoring: application to Morocco. *International Journal of Remote Sensing, 21*, 353-366

Tobin, D.C., Revercomb, H.E., Knuteson, R.O., Lesht, B.M., Strow, L.L., Hannon, S.E., Feltz, W.F., Moy, L.A., Fetzer, E.J., & Cress, T.S. (2006). Atmospheric Radiation Measurement site atmospheric state best estimates for Atmospheric Infrared Sounder temperature and water vapor retrieval validation. *Journal of Geophysical Research-Atmospheres, 111*, -

Valor, E., & Caselles, V. (1996). Mapping land surface emissivity from NDVI: Application to European, African, and South American areas. *Remote Sensing of Environment, 57*, 167-184
Vandegriend, A.A., & Owe, M. (1993). On the Relationship between Thermal Emissivity and the Normalized Difference Vegetation Index for Natural Surfaces. *International Journal of Remote Sensing, 14*, 1119-1131